Journal of Materials Chemistry A

ROYAL SOCIETY OF CHEMISTRY

PAPER

View Article Online
View Journal

Check for updates

Cite this: DOI: 10.1039/d6ta00453a

The role of oxygen excess on fluoride intercalation in Ruddlesden–Popper electrodes for fluoride ion batteries: the case of $LaSrMnO_4$

Gabriele Mezzadra,[a] Xiangwei Guo,[b] Marco Ravalli,[a] Clemens Ritter,[c] Davide Ceresoli,[d] Oliver Clemens[b] and Cristina Tealdi*[a]

Received 16th January 2026
Accepted 1st March 2026

DOI: 10.1039/d6ta00453a

rsc.li/materials-a

Ruddlesden–Popper-type compounds are particularly attractive electrode materials for fluoride-ion batteries. Among them, $LaSrMnO_4$ has received significant attention due to its high fluoride incorporation capability and lower environmental impact compared to nickel- and cobalt-based analogues. In this work, neutron diffraction data are used to provide an experimental visualization of fluoride-ion diffusion in this class of materials, through maximum entropy method (MEM) and bond valence site energy (BVSE) analysis. Additionally, since oxygen excess is well known in Ruddlesden–Popper oxides but its impact on fluoride-ion transport has not been previously investigated, molecular dynamics (MD) simulations were employed to reveal how oxygen over-stoichiometry affects fluoride intercalation mechanisms and energetics, unveiling new migration pathways that hinder fluoride mobility. These findings have direct implications for fluoride-ion battery performance, highlighting the critical role of oxygen content in determining anion transport and the electrochemical performance of this class of materials.

Open Access Article. Published on 12 March 2026. Downloaded on 4/3/2026 5:12:45 PM.
This article is licensed under a Creative Commons Attribution-NonCommercial 3.0 Unported Licence.

1 Introduction

Lithium-ion batteries (LIBs) have dominated the portable energy storage market since their commercial introduction in the early 1990s. However, LIBs also have notable drawbacks. These include the high cost and limited availability of lithium resources, potential safety issues related to thermal runaway, and environmental concerns associated with the mining and disposal of lithium and other critical materials used in these batteries.[1–3] This has led to the exploration of alternative battery chemistries. Among these emerging technologies, fluoride-ion batteries (FIBs) stand out for their significant potential. They could theoretically surpass LIBs in both gravimetric and volumetric energy densities.[4,5] Moreover, fluorine is the 13th most abundant element in the Earth's crust and is widely distributed, with major producers across four continents.[6] This abundant and well-established supply chain makes fluorine a highly promising candidate for developing FIBs as a cost-effective alternative to Li-ion battery technologies. Nevertheless, the handling and processing of large quantities of fluorine precursors required for mass-scale production may pose practical and safety challenges that must be carefully addressed.

FIBs are still a largely unexplored technology, with the choice and optimization of materials to be used as electrodes and electrolytes at a starting stage. The potential of FIBs for reversible energy storage was first proven using cells with conversion-based electrode materials, which use the conversion of a metal into its fluorinated phase. However the poor electrochemical stability of these materials during cycling has led to the exploration of intercalation-based electrodes where guest ions are inserted into normally unoccupied interstitial sites or anion vacancies in the stable host material's crystal structure.[4,5] This strategy offers a significant advantage: ions can be inserted or removed with minimal volume changes during redox reactions, while the fundamental crystal framework of the host material remains largely intact. Among these materials, compounds with the Ruddlesden–Popper-type structure, with general formula $A_{n+1}B_nX_{3n+1}$ have emerged as the most promising candidates.

Several compounds from the Ruddlesden–Popper oxide family have been investigated, including La_2NiO_4,[7,8] La_2CoO_4,[9] and $LaSrMnO_4$ (ref. 10 and 11) for $n = 1$ family, whose structure consists of alternating ABX_3 perovskite layers and AX rock-salt subunits stacked along the c-axis, as well as $La_{1.2}Sr_{1.8}Mn_2O_7$ (ref. 12 and 13) for the $n = 2$ counterparts in which two connected perovskite layers are separated by a single rock-salt layer. The $n = 1$ family has demonstrated the most promising

[a]Department of Chemistry, University of Pavia, via Taramelli 12, Pavia, 27100, Italy. E-mail: cristina.tealdi@unipv.it

[b]University of Stuttgart, Institute for Materials Science, Materials Synthesis Group, Heisenbergstraße 3, Stuttgart, 70569, Germany. E-mail: oliver.clemens@imw.uni-stuttgart.de

[c]Institut Laue-Langevin, 71 Avenue des Martyrs, Grenoble, 38042, France

[d]Istituto di Scienze e Tecnologie Chimiche "Giulio Natta" (SCITEC) del Consiglio Nazionale delle Ricerche (CNR), via C. Golgi, 19, Milano, 20133, Italy

Open Access Article. Published on 12 March 2026. Downloaded on 4/3/2026 5:12:45 PM. This article is licensed under a Creative Commons Attribution-NonCommercial 3.0 Unported Licence.

performance, offering higher theoretical capacities and thus energy densities than the $n = 2$ counterpart. Among these materials, $LaSrMnO_4$ stands out for its high fluoride incorporation capability and the lower environmental impact compared to nickel- and cobalt-based analogues.[11]

The structure of $LaSrMnO_4$ consists of alternating layers of (La/Sr)MnO_3 perovskite and (La/Sr)O rock-salt subunits along the *c*-axis, resulting in a tetragonal symmetry (space group *I*4/*mmm*). Strontium and lanthanum are randomly distributed within the same crystallographic site. The F^- ions occupy the interlayer gaps of the (La/Sr)O rock-salt subunits that separate the perovskite like blocks. Within this configuration, each fluoride ion has four nearest and four next-nearest F^- neighbours forming a two-dimensional sublattice of potential hopping sites.

The fluorination process proceeds stepwise, initially forming $LaSrMnO_4F_1$, where all interstitial sites within one layer are fully occupied while the adjacent layer remains vacant, leading to a reduction in symmetry from *I*4/*mmm* to *P*4/*nmm*. As fluorination continues and all interstitial sites in every layer become filled, the overall composition becomes close to $LaSrMnO_4F_2$ indicating that the structure can ideally accommodate two fluoride ions per formula unit.[15] When the second layer is fully occupied, the symmetry is restored to *I*4/*mmm* (Fig. 1).[14] In our previous work,[11] the phase stability of fluorinated compositions was investigated through a formation energy convex hull of the $LaSrMnO_4F_x$ system ($0 < x < 2$). This analysis allowed the identification of several stable intermediate compositions and supported the experimental observation that fluorination proceeds through both monophasic and biphasic regions, depending on the overall fluorine content. A solid solution domain is predicted between $LaSrMnO_4F_{\sim 0.75}$ and $LaSrMnO_4F_1$ and between $LaSrMnO_4F_{\sim 1.8}$ and $LaSrMnO_4F_2$. That study also reported the first molecular dynamics simulations conducted for this system, focusing on the $LaSrMnO_4F_{0.9}$ composition at 450 K. The simulations revealed that fluoride ions are the only species exhibiting long-range diffusion under operating conditions. Ion diffusion occurs *via* vacancy hopping between nearest neighbour F sites along the ⟨110⟩ directions. This diffusion is confined to the fluoride interstitial layers, with no evidence of interlayer transport, predicting a two-dimensional nature of fluoride ion conduction in these materials.

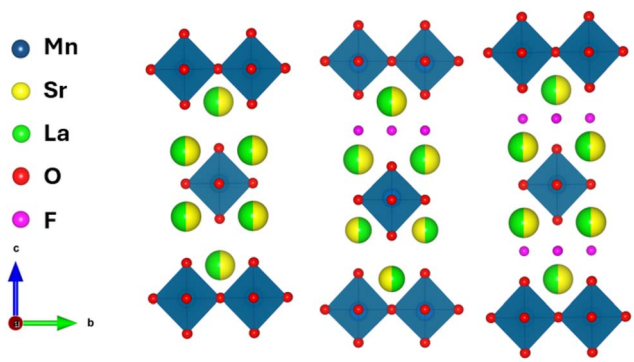

Fig. 1 Crystal structure of $LaSrMnO_4$ (*I*4/*mmm* space group) and its fluorination process (from left to right). Fluoride ions first occupy all interstitial sites in alternating layers, forming $LaSrMnO_4F_1$ and reducing symmetry to *P*4/*nmm*. As fluorination proceeds and all layers are filled, the composition reaches $LaSrMnO_4F_2$, restoring the *I*4/*mmm* symmetry.[14]

However, a direct experimental visualization of the diffusion pathways in this system is required to validate and correlate with computational predictions. To address this, we performed maximum entropy method (MEM) and bond valence site energy (BVSE) analyses to experimentally probe the anion distribution and identify possible diffusion pathways within this system. To gain deeper insight into the fluoride-ion diffusion mechanism and energetics, molecular dynamics simulations were carried out at different temperatures. In addition, our previous work[11] employed iodometric titration to estimate the oxygen content of $LaSrMnO_4$, revealing a slight oxygen over-stoichiometry in the sample. While oxygen excess is a well-known phenomenon in Ruddlesden–Popper oxides,[16,17] its influence on fluoride diffusion has never been systematically explored. To fill this gap, additional simulations were performed in the present work to assess how oxygen over-stoichiometry may affect anion transport in this class of materials.

2 Experimental section

2.1 Material synthesis

$LaSrMnO_4$ was synthesized *via* a solid-state reaction. Stoichiometric amount of La_2O_3 (Alfa Aesar, 99.9%, pre-dried at 1000 °C for 12 h before use), $SrCO_3$ (Sigma-Aldrich, 99.99%), Mn_2O_3 (Sigma-Aldrich, 99.99%) were hand milled with mortar and pestle. Then the mixture was heated up to 1100 °C for 6 h followed by second heating at 1450 °C for 40 h with one intermediate grinding under flowing Argon (99.9%, 0.5 SLM (standard liter per minute) flow). The heating and cooling rates were 2 and 1 °C min^{-1}, respectively. For the chemical fluorination AgF (Sigma-Aldrich, 99%) was used as solid-state oxidizing agent, according to the reaction presented below (eqn (1)). The two reactants were hand milled using mortar and pestle in an Argon-filled glovebox. The fluorination was conducted at 250 °C for 48 h in a stainless-steel ampoule sealed with static argon inside.

$$LaSrMnO_4 + xAgF \rightarrow LaSrMnO_4F_x + xAg \quad (1)$$

2.2 Structural characterization

Neutron powder diffraction (NPD) patterns were acquired on pure and fluorinated compounds at the high resolution two axis diffractometer D2B at the Institut Laue Langevin (ILL). Data were acquired with an incident wavelength of 1.5939 Å at room temperature (RT) and 150 °C respectively for the oxide compound as well as at RT, 150 °C and 300 °C respectively for the fluorinated phase. All samples were measured in air inside quartz tubes in the 0–158° 2θ range. A separate measurement of an empty quartz tube was also performed to subtract its contribution to the background. NPD data were analysed *via* Rietveld analysis using the TOPAS v6 software.[18] The

Open Access Article. Published on 12 March 2026. Downloaded on 4/3/2026 5:12:45 PM. This article is licensed under a Creative Commons Attribution-NonCommercial 3.0 Unported Licence.

background was modelled with a Chebyshev polynomial function with four coefficients. A zero-shift correction was applied to account for peak displacement, and the Lorentz–polarization (LP) factor was refined for intensity corrections. Sample related peak broadening was described by pseudo-Voigt functions. Anisotropic strain broadening was modelled using the Stephens model for the tetragonal space group. Thermal displacement parameters were refined for all atom types; for lanthanum and strontium (each with 0.5 occupancy at the same crystallographic position), they were constrained to be identical.

The refined structural models obtained from Rietveld analysis served as the foundation for further investigations using the maximum entropy method (MEM) and bond valence site energy (BVSE) approaches. The MEM was employed using the ERIS software[19] to obtain real space scattering length density maps from the refined structure factors. MEM reconstructs the most probable nuclear density distribution consistent with the observed diffraction data. By combining both the real and imaginary components of the observed structure factors and their uncertainties, MEM provides a detailed picture of the spatial distribution of atoms and dynamic disorder within the lattice. To perform MEM analysis the unit cell was divided into $128 \times 128 \times 128$ pixels.

Complementary to MEM, the BVSE method was employed using the softBV software[20] to estimate the energy landscape associated with ion diffusion by applying a Morse-type force field. This semi-empirical approach quantifies the energetic cost for a mobile ion to occupy different crystallographic positions, thereby identifying the most favourable diffusion pathways and potential bottlenecks. The resulting three-dimensional energy isosurfaces provide a map of the potential migration channels within the crystal structure. Visualization of MEM and BVSE results were performed using VESTA.[21]

2.3 Computational methods

In our previous work[11] pretrained machine learning (ML) interatomic potentials were employed to model interactions between ions in the system. In particular, the MACE-MP-0b3 medium model[22] was tested and demonstrated high accuracy in describing the structural and dynamical properties of $LaSrMnO_4$ based compounds. The model successfully captured the lattice parameter changes induced by fluorination, with deviations from experimental values of less than 3%. In addition to accurately reproducing lattice parameters, the model effectively predicted variations in manganese oxygen bond lengths during the fluorination process. Beyond its accuracy, this ML based approach offers greater flexibility compared to density functional theory (DFT), allowing simulations of larger systems, longer timescales, and the possibility to handle ions in random or partially disordered positions within the lattice. In the present study, molecular dynamics simulations were carried out using the same interatomic potential, which has been shown to accurately capture both the structural and dynamical properties of the system.

Energy minimization calculations were carried out in an orthogonal simulation box under periodic boundary conditions using the LAMMPS code.[23] Energy minimization is essential to calculate the total energy of a system, and can be used to compare the structural stability of different arrangements. The simulation box consisted of $6 \times 6 \times 2$ unit cells, generated from the tetragonal $P4/nmm$ structure, resulting in supercells containing approximately 1100 atoms, depending on the specific composition. To avoid imposing artificial symmetry constraints during the calculations, the supercells were geometrically optimized in $P1$ symmetry at 0 K and 1 atm using the conjugate gradient minimization algorithm. Fluoride ion vacancies were introduced following a stepwise distribution, with one layer fully vacant and the adjacent layer containing randomly distributed vacancies. This configuration is consistent with experimental observations.[14]

Molecular dynamics (MD) simulations were then performed using the LAMMPS code[23] to investigate the diffusion mechanisms of fluoride ions within the system. Each configuration was first equilibrated in the isothermal–isobaric (*NPT*) ensemble for 20 ps using the Nosé–Hoover thermostat and the Velocity–Verlet integration scheme to determine the equilibrium cell volume at various temperatures under a pressure of 1 atm. Subsequently, production runs were carried out in the canonical (*NVT*) ensemble for 400 ps, employing the same thermostat and integration algorithm, with a time step of 1 fs. Ion trajectories and diffusion pathways were analysed using the VMD[24] software package, while the mean squared displacement (MSD) and related diffusion properties were calculated using the MDANSE software.[25]

In our previous work,[11] we evaluated the phase stability of the $LaSrMnO_4F_x$ system ($0 < x < 2$). Compositions between $LaSrMnO_4F_{0.75}$ and $LaSrMnO_4F_1$ were found to be stable, in line with experimental evidence. In the present study, we chose to simulate the $LaSrMnO_4F_{0.8}$ composition to maximize the number of fluoride vacancies in the system, a critical parameter for studying fluoride-ion diffusion. Three different compositions were simulated to explore the role of fluorine content and oxygen over stoichiometry: $LaSrMnO_4F_{0.8}$, $LaSrMnO_{4.1}F_{0.8}$ and $LaSrMnO_{4.2}F_{0.8}$. The simulations were conducted at temperatures ranging from 300 K to 700 K, in increments of 50 K, for a total of nine distinct temperature conditions analysed.

3 Results and discussions

The room temperature neutron powder diffraction (NPD) pattern of $LaSrMnO_4$ is shown in Fig. 2(a). No additional diffraction peaks were observed, confirming that the sample is phase pure and crystalline, with no detectable impurity phases. Structural refinement was performed using the previously reported $I4/mmm$ space group; the results are summarized in Table S1(a). The Rietveld-refined lattice parameters are in good agreement with previously reported literature.[14] Within the structure, oxygen atoms exhibit the highest thermal factors in the system. Notably, the apical oxygen atoms in the MnO_6 octahedra show larger isotropic thermal displacements compared to the equatorial oxygens. This observation aligns with literature findings, as apical oxygens are known to possess higher mobility and tend to diffuse at elevated temperatures in

Open Access Article. Published on 12 March 2026. Downloaded on 4/3/2026 5:12:45 PM.
This article is licensed under a Creative Commons Attribution-NonCommercial 3.0 Unported Licence.

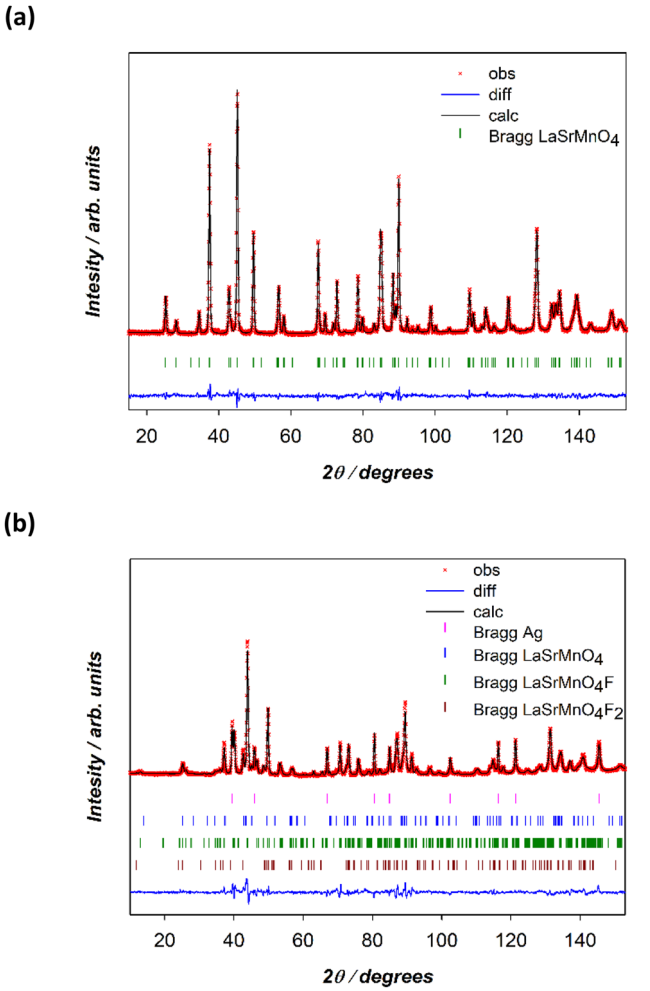

Fig. 2 Room temperature neutron powder diffraction (NPD) pattern of $LaSrMnO_4$ (a) and the corresponding fluorinated phase (b). No additional diffraction peaks were observed in the oxide phase, confirming that the sample is phase-pure and crystalline. In the fluorinated phase four phases are present: metallic silver, originating from the reaction between $LaSrMnO_4$ and AgF, the expected $LaSrMnO_4F$ phase, and two minor impurity phases, unreacted $LaSrMnO_4$ and $LaSrMnO_4F_2$, each contributing less than 5%. Simulated Bragg peak positions for all phases are indicated by colored ticks.

this class of materials.[26,27] A similar trend in isotropic thermal displacement values was observed in the NPD pattern collected at 150 °C (Table S1(b)).

The room temperature NPD pattern of the fluorinated phase is shown in Fig. 2(b). Four distinct phases were identified: metallic silver, originating from the reaction between $LaSrMnO_4$ and AgF (according to (eqn (1)), the expected $LaSrMnO_4F$ phase and two minor impurity phases, unreacted $LaSrMnO_4$ and $LaSrMnO_4F_2$, each contributing less than 5%. The presence of unreacted $LaSrMnO_4$ indicates incomplete fluorination, whereas the $LaSrMnO_4F_2$ impurity suggests localized over fluorination, reflecting an overall inhomogeneous fluorination process.

As the measurement temperature increases to 150 °C and 300 °C, the fractions of $LaSrMnO_4$ and $LaSrMnO_4F_2$ decrease, while that of $LaSrMnO_4F$ increases, as summarized in Table S1(c)–(e). The apparent increase in the Ag fraction at higher temperatures probably arises from residual traces of AgF that remain in the sample but are below the detection limit. After excluding the contribution of metallic silver, which displays sharp and well resolved peaks distinct from those of the $LaSrMnO_4F_x$ phases, the relative phase fractions were rescaled, revealing that $LaSrMnO_4F$ constitutes more than 85 wt% of the total composition. Initial indexing and refinement of the nominal $LaSrMnO_4F$ phase were performed in the tetragonal $P4/nmm$ space group. However, discrepancies between observed and calculated reflections suggested the need to explore alternative structural models (Fig. S1). The best agreement was achieved using the monoclinic $C2/m$ space group to describe the $LaSrMnO_4F$ composition. This lower symmetry arises from a distortion of the MnO_6 octahedra, particularly a change in the angle between the two apical oxygen atoms (O2 and O3) and the central Mn atom. In the $P4/nmm$ structure, this angle is 180°, while in the $C2/m$ structure it distorted to 177.4°, leading to an overall reduction in symmetry (Fig. S2). This transformation corresponds to a *klassengleiche* (k-type) subgroup relationship. Specifically, the transition from the tetragonal $P4/nmm$ to the monoclinic $C2/m$ structure involves both a change in the lattice type and a reduction in the number of symmetry operations. Similar symmetry lowering distortions have also been reported in related Ruddlesden–Popper oxyfluorides, such as $La_2CoO_4F_{1.2}$ ($P2_1/c$) and $La_2NiO_3F_2$ ($C2/c$).[7,9]

By monitoring the variation of the lattice parameters with temperature, a thermal expansion coefficient of $31.9 \times 10^{-6}\ K^{-1}$ was determined. The refinement of the fluoride site occupancy resulted in a value of 0.95(2), corresponding to a composition of $LaSrMnO_4F_{0.95}$. A similar trend to that observed in $LaSrMnO_4$ is found for the isotropic thermal displacement parameters: the anions exhibit the highest thermal mobility and the apical oxygen atoms show larger thermal displacements than the equatorial ones. In this fluorinated compound further differentiation can be made between the two apical oxygens. One oxygen atom lies adjacent to the fluorine layer, while the other is located near an empty layer. Additionally, the two apical oxygens differ in their distances to the Mn atom due to the Jahn–Teller distortion of Mn^{4+}. The oxygen atom near the F^- layer exhibits a higher isotropic thermal displacement, likely because the presence of the fluorine layer perturbs its local environment. However, across all investigated temperatures, the fluoride ions exhibit the largest thermal displacement parameters, as expected for their lighter mass and higher mobility.

The structural models obtained from Rietveld refinement served as the foundation for further investigations using MEM. Both the real and imaginary components of the observed structure factors, along with their corresponding uncertainties for each reflection, were used to perform MEM analysis. Fig. 3(a)–(c) shows the anion scattering length distributions obtained from the MEM analysis at room temperature, 150 °C and 300 °C. At room temperature, the nuclear density is well centred around the atomic positions, indicating localized anions with limited thermal motion. As the temperature

 This journal is © The Royal Society of Chemistry 2026

Open Access Article. Published on 12 March 2026. Downloaded on 4/3/2026 5:12:45 PM.
This article is licensed under a Creative Commons Attribution-NonCommercial 3.0 Unported Licence.

increases, the anion nuclear density becomes progressively broader, extending further from the equilibrium atomic sites. This broadening reflects enhanced atomic vibrations and increased anion mobility, consistent with the trend observed in the isotropic thermal displacement parameters obtained from the Rietveld refinement. The corresponding planar projections of the MEM maps, focusing exclusively on the fluoride ions, are also presented in Fig. 3(d) and (e). As previously discussed, the F^- ions occupy the interlayer gaps that separate the perovskite like blocks. Within this configuration, each fluoride ion has four nearest F^- neighbours and four F^- next-nearest neighbours, forming a two-dimensional sublattice of potential hopping sites. Based on the crystallographic geometry, two principal diffusion pathways for fluoride motion can be identified: hopping between nearest neighbour F^-, and towards next-nearest neighbours. These pathways represent the most plausible routes for fluoride intercalation and deintercalation within the layered framework.

In the tetragonal *P*4/*mmm* structure, the predicted hopping direction is ⟨110⟩, corresponding to the shortest path between nearest neighbour F^- ions. However, since the MEM analysis was performed in the refined monoclinic *C*2/*m* space group, a transformation between the two settings was necessary. In this conversion, the diagonal of the *C*2/*m* basal plane corresponds to the *a*/*b* lattice vector of the tetragonal *P*4/*mmm* cell. This relationship reflects the transformation from the higher-symmetry *P*4/*mmm* parent structure to the lower symmetry *C*2/*m* derivative and ensures that equivalent crystallographic directions and atomic positions are properly aligned for comparison. Consequently, the predicted fluoride-ion diffusion along the ⟨110⟩ direction in the *P*4/*mmm* is mapped onto the ⟨100⟩ and ⟨010⟩ directions in *C*2/*m* based simulations (Fig. S3). At room temperature, the MEM map reveals an almost isotropic distribution of F^- scattering length in the *ab*-plane. The fluoride ions appear well localized around their crystallographic positions, suggesting that at low temperature they remain confined, with minimal dynamic disorder. Upon heating to 300 °C, the MEM results show a broadening of the F^- scattering length distribution. The distribution becomes increasingly anisotropic, with an elongation along the ⟨010⟩ and ⟨100⟩ directions where adjacent fluoride ions are located. This expansion of the scattering density is indicative of enhanced thermal motion and partial delocalization of the fluoride ions within the conduction layer. Such temperature dependent broadening is consistent with an increase in anionic mobility driven by thermal activation. However, despite the indications of increasing mobility, a fully resolved image of fluoride diffusion from the MEM data alone was not achievable. This limitation arises primarily from the low concentration of vacancy sites, as the refined occupancy of fluoride ions in the interstitial positions is 0.95(2) (Table S1). Such a small number of vacancies is insufficient to enable a clear experimental observation of ion diffusion. In addition, the relatively narrow temperature range investigated further restricts the ability to capture dynamic diffusion behaviour, as higher temperatures would likely enhance ion mobility and provide a more distinct visualization of the diffusion pathways; however, the thermal stability of the oxyfluoride is limited and would need to be considered to avoid decomposition.

To gain deeper insight into the possible F^- migration mechanisms, BVSE calculations were subsequently performed. Fig. 3(f) shows the combination of MEM analysis with BVSE results. Both analyses converge on a consistent picture: the

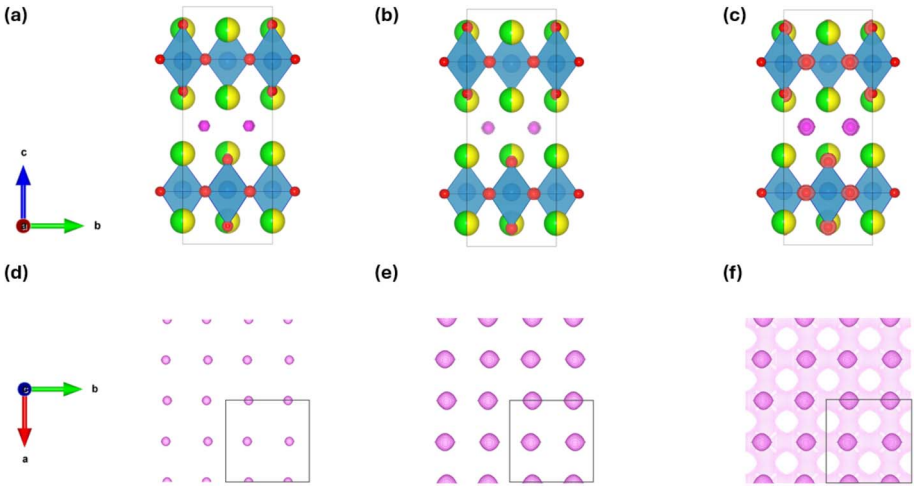

Fig. 3 Anion scattering length distributions obtained from MEM analysis at room temperature (a), 150 °C (b), and 300 °C (c). Oxide related isosurfaces are shown in red while fluoride related isosurfaces in purple. With increasing temperature, the anion nuclear density broadens and extends further from the equilibrium atomic positions, reflecting enhanced atomic vibrations and increased anion mobility. Planar projections of the MEM maps focusing exclusively on fluoride related isosurfaces, at RT (d) and 300 °C (e). At room temperature, the MEM map reveals an almost isotropic distribution of F^- scattering length in the *ab*-plane. Upon heating to 300 °C, the MEM results show a broadening of the F^- scattering length distribution. The distribution becomes increasingly anisotropic, with an elongation along the ⟨010⟩ and ⟨100⟩ directions where adjacent fluoride ions are located. Panel (f) combines the 300 °C MEM results with BVSE calculations, showing that both methods consistently indicate preferred fluoride-ion diffusion along these directions within the *ab* plane.

Open Access Article. Published on 12 March 2026. Downloaded on 4/3/2026 5:12:45 PM.
This article is licensed under a Creative Commons Attribution-NonCommercial 3.0 Unported Licence.

preferred migration of fluoride ions occurs along the ⟨100⟩ and ⟨010⟩ directions within the *ab*-plane, corresponding to the directions where elongation of the MEM derived scattering density was observed. Importantly, these directions form a continuous diffusive network within the structure and are therefore expected to support long-range F^- diffusion. The BVSE calculations predict an activation energy of approximately 0.9 eV for ion diffusion along these directions, suggesting relatively hindered diffusion in the system. In contrast, neither method indicates any significant probability of diffusion along the ⟨110⟩ direction toward second nearest neighbours, in agreement with our previous work.[11]

The experimental evidence obtained through the combined use of MEM and BVSE analyses was further supported by molecular dynamics simulations on the $LaSrMnO_4F_{0.8}$ composition. The simulation supercells were generated from the tetragonal *P*4/*nmm* unit cell. To avoid imposing artificial symmetry constraints, the supercells were geometrically optimized in *P*1 symmetry. This approach allowed the octahedra to freely tilt during energy minimization, reproducing the characteristic distortion of the MnO_6 units observed in the *C*2/*m* structure.

By monitoring the expansion of the supercell lattice parameters at different temperatures during the NPT simulations (Table S2), a simulated thermal expansion coefficient of 59.7×10^{-6} K^{-1} was obtained, in reasonable agreement with the experimental value of 31.9×10^{-6} K^{-1} derived from neutron diffraction measurements in this study, further validating the accuracy of the model. The mean squared displacement (MSD) of each atom type in $LaSrMnO_4F_{0.8}$ was evaluated at all simulated temperatures (Fig. 4(a) shows as an example the results obtained at 700 K), revealing that fluoride ions are the only species exhibiting long range diffusion. Notably, only one type of hopping is predicted: between nearest neighbour F^- ions (Fig. 4(b)), in agreement with experimental observations and in line with our previous investigation. As expected for a thermally activated hopping mechanism, fluoride diffusion increases with temperature; this trend is reflected in the growth of the MSD values and the corresponding diffusion coefficients. By plotting the diffusion coefficients as a function of temperature in an Arrhenius plot, the activation energy for fluoride ion diffusion was determined to be 0.14 eV (Fig. 4(c)).

Although direct experimental measurements of fluoride ion diffusion in closely related systems remain limited, low migration barriers are plausible for fluorinated frameworks in which mobile anions occupy interstitial or weakly bound sites. In this context, the relatively low energy activation predicted here may be related to the presence of fluoride ions in interstitial environments that facilitate hopping. For comparison, we recall that activation energies for interstitial oxide ion diffusion in La_2MO_{4+d} (M = Ni, Co) as low as 0.12–0.19 eV were reported for epitaxial thin films; slightly higher values in the range 0.31–0.41 eV were derived from MD on the same compositions.[28]

However, this value differs significantly from the migration energy predicted by BVSE calculations. This discrepancy arises because BVSE is a static, geometry-based approach that estimates migration energies based on idealized bond valence sums and site energies, without accounting for dynamic effects, thermal vibrations, or the collective motion of ions; moreover, the approach doesn't consider effective lattice relaxation

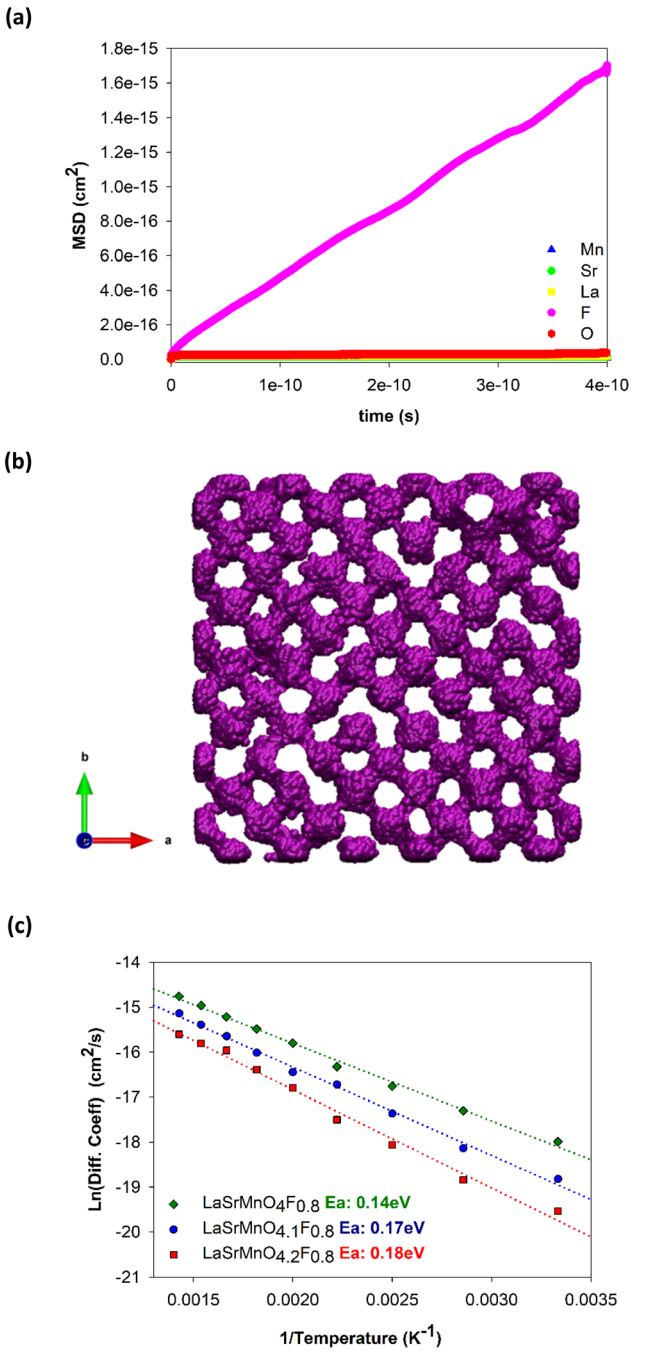

Fig. 4 (a) Mean squared displacement (MSD) at 700 K for $LaSrMnO_4F_{0.8}$ obtained from MD simulations. A zoom of the initial part of the simulation with fluoride ions omitted is presented in the SI (Fig. S4). Fluoride ions show long range diffusion, while oxygen exhibits the highest vibrational motion among immobile species; manganese is the least mobile, and strontium and lanthanum show similar displacements. (b) Planar projections of fluoride trajectories derived from MD simulations at 700 K. In the tetragonal *I*4/*mmm* structure, the predicted hopping direction is ⟨110⟩, corresponding to the shortest path between nearest neighbour F^- ions. (c) Arrhenius plots of fluoride diffusion for $LaSrMnO_4F_{0.8}$, $LaSrMnO_{4.1}F_{0.8}$ and $LaSrMnO_{4.2}F_{0.8}$. The corresponding activation energies are 0.14 eV, 0.17 eV, and 0.18 eV, respectively.

Open Access Article. Published on 12 March 2026. Downloaded on 4/3/2026 5:12:45 PM.
This article is licensed under a Creative Commons Attribution-NonCommercial 3.0 Unported Licence.

around defects. In contrast, molecular dynamics simulations explicitly incorporate atomic motions, temperature effects, and interactions between mobile ions and the lattice over time. As a result, MD can capture realistic hopping events, making it a more accurate and reliable method for quantifying activation energies and diffusion coefficients. Consequently, while BVSE provides a useful qualitative map of possible diffusion pathways, it tends to overestimate energy barriers and cannot fully capture the temperature dependent kinetics observed in MD simulations. Moreover, MD offers a key advantage over BVSE: it enables the study of structural complexity and disorder, such as partial occupancies, local distortions, or off-stoichiometric compositions, which cannot be handled reliably by static methods.

As previously discussed, oxygen over-stoichiometry is a common feature in Ruddlesden–Popper-type materials.[28–30] For example, in our previous work, iodometric titration was employed to determine the oxygen stoichiometry of the sample prepared under identical conditions to this study, revealing a composition of $LaSrMnO_{4.06}$. The effect of oxygen over-stoichiometry on fluoride diffusion in this class of materials has never been investigated. To address this gap, additional supercells were constructed and analysed to explore how excess oxygen may influence anion transport behaviour.

Three possible configurations were considered to identify the most favourable location for accommodating the excess oxygen within the fluorinated structure. In the first configuration, excess oxygen was placed exclusively in the empty interlayer regions; in the second, it was confined to the fluoride occupied layers; and in the third, oxygen atoms were evenly distributed across all layers. After structural relaxation performed as described in Section 2.3, the third scenario, where oxygen atoms are uniformly distributed between the layers, was found to be the most energetically favourable; in fact, the total energy of this configuration was calculated to be approximately 0.05 eV per formula unit lower than the total energy of the other two arrangements. Based on this result, two oxygen-rich compositions were subsequently constructed and analysed: $LaSrMnO_{4.1}F_{0.8}$ and $LaSrMnO_{4.2}F_{0.8}$.

The simulation conducted on the oxygen over-stoichiometric samples at temperatures close to room temperature (*i.e.*, below 450 K), showed a diffusion mechanism for F^- ions in line with the data shown for the $LaSrMnO_4F_{0.8}$ composition. Interestingly, in $LaSrMnO_{4.1}F_{0.8}$, not only fluoride ions but also oxide ions exhibit mobility at simulated temperatures above 450 K. Both interstitial and apical oxygen atoms display measurable mobility, whereas equatorial oxygens remain immobile, consistent with the isotropic thermal displacements obtained from Rietveld refinements (Table S1). Three distinct types of oxygen motion were observed in the oxygen-rich compositions. The first occurs along the ⟨110⟩ direction, the same pathway used by fluoride ions. The second involves layers without fluoride, where interstitial oxygen replaces an apical oxygen, which then moves into a nearby interstitial site. The third mechanism occurs within fluoride occupied layers: fluoride ions can substitute apical oxygen atoms, which are moved into interstitial positions. At the end of this process, the apical site is occupied by a fluoride ion, while an oxide ion occupies an interstitial position (Fig. 5). This configuration is significantly important because at the end of the process a fluoride ion is trapped in the apical site of the octahedra while a slower oxide ion resides in the fluoride layer, reducing the overall mobility of charge carriers.

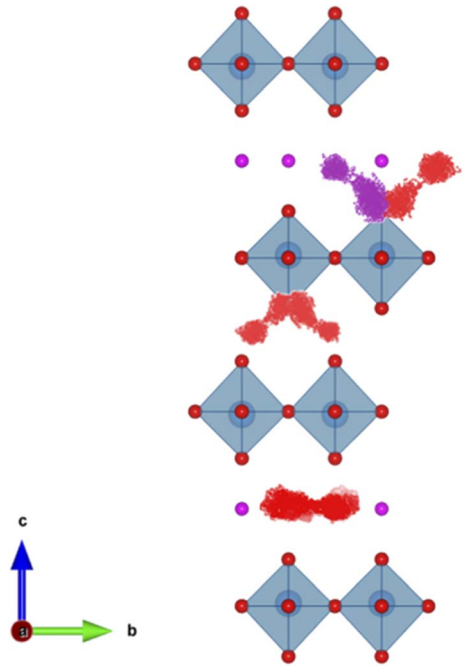

Fig. 5 Schematic representation of the three oxide ion migration mechanisms in oxygen over stoichiometric compositions: along ⟨110⟩ (same pathway as fluoride in the system without oxygen excess), in fluoride-free layers *via* interstitial–apical exchange, and in fluoride-occupied layers where fluoride substitutes apical oxygen displacing it to an interstitial site.

All three types of oxygen motion are characteristic of oxygen-rich compositions, such as $LaSrMnO_{4.1}F_{0.8}$. The reasons for this exclusivity differ for each mechanism. The first two types are possible only in oxygen-rich compounds because the excess oxygen occupies interstitial sites, whereas in $LaSrMnO_{4.0}F_{0.8}$, all oxygen atoms are confined within the MnO_6 octahedra, and the energy required for them to leave these sites is prohibitively high at low temperatures.

For the third type of oxygen motion, the reason why it is exclusively present in oxygen-rich compositions is more complex. In both the stoichiometric and oxygen-excess compounds, fluoride ions occupy interstitial sites; however, based on the current analysis, only in the oxygen-excess materials fluoride ions can substitute apical oxygen atoms, which are moved into interstitial positions. The larger size and higher charge of interstitial oxide ions, relative to interstitial fluoride, likely perturbs the fluoride planes, promoting their substitution at apical oxygen atoms positions.

However, at the simulated temperatures oxygen motion remains confined to localized jumps and does not develop into long-range diffusion. These localized jumps involve only short-range displacements that allow site exchanges, whereas long-

Open Access Article. Published on 12 March 2026. Downloaded on 4/3/2026 5:12:45 PM.
This article is licensed under a Creative Commons Attribution-NonCommercial 3.0 Unported Licence.

range diffusion would correspond to displacements on the order of several Å across the lattice. Notably in Ruddlesden–Popper phases oxide ions exhibit long-range diffusion only at significantly higher temperatures.[29] This is also an important finding in the light of a recent study of Aalto *et al.*[31] who found that oxygen release of electrochemically fluorinated materials such as $La_2NiO_{4+d}F_{2-d-x}$ under formation of lower oxide content phases $La_2NiO_{4+d-y}F_{2-d-x}$ ($+y/2$ O_2) requires further thermal activation at least at temperature higher than 523 K in order to proceed. Thus, the low Fermi levels introduced by oxidative chemical or electrochemical fluorination, which can oxidize oxide ions and cause oxygen loss, must be considered to become at least partially facilitated by the reduced mobility of oxide ions compared to the inserted fluoride species, and this findings indicate that the type of transition metal as well as the composition of the A-site lattice has only limited influence on this aspect.

The $LaSrMnO_{4.1}F_{0.8}$ composition exhibits a lower fluoride diffusion coefficient and a higher activation energy compared to $LaSrMnO_4F_{0.8}$ (Fig. 4(c)). This reduction in fluoride mobility arises from two factors: the lower concentration of vacancies available for hopping (as some of them are filled by the excess oxygen in the structure) and the trapping of fluoride ions in apical octahedral sites while a slower oxide ion resides in the fluoride layer. Finally, increasing the oxygen content further, as in $LaSrMnO_{4.2}F_{0.8}$, leads to an even lower average fluoride diffusion coefficient and higher activation energy. This behaviour is attributed to the further reduction in available vacancy sites and an increased frequency of fluoride trapping, although the fundamental diffusion mechanism remains unchanged from that observed in $LaSrMnO_{4.1}F_{0.8}$.

The reported results could have significant implications for the performance of electrochemical cells during operation. First, the presence of excess oxygen in the cathode material reduces the number of available sites for fluoride incorporation, thereby decreasing the overall capacity of the cathode. In addition, oxygen atoms can obstruct the diffusion pathways for fluoride ions, leading to slower ionic transport and an increased overpotential during cell operation. This effect is particularly relevant under realistic operating conditions. For instance, simulations performed at 450 K, a temperature representative of typical cell operation,[5,8,9,11,13,14] show that the fluoride diffusion coefficient decreases substantially with increasing oxygen content. Specifically, the diffusion coefficient drops from 8.12×10^{-8} cm^2 s^{-1} in $LaSrMnO_4F_{0.8}$ to 5.47×10^{-8} cm^2 s^{-1} in $LaSrMnO_{4.1}F_{0.8}$, and further to 2.5×10^{-8} cm^2 s^{-1} in $LaSrMnO_{4.2}F_{0.8}$. These results indicate that even small amounts of oxygen over-stoichiometry can significantly impede fluoride mobility, potentially limiting the electrochemical performance of the material and affecting the overall efficiency and lifespan of the cell. The results are particularly significant in that $LaSrMnO_4$-based intercalation materials are less prone to accommodate oxygen over-stoichiometry compared to the isostructural compounds La_2NiO_4 and La_2CoO_4, for which the implications of the presence of excess oxygen on the performance of electrochemical cells during operation could be even more severe and warrant further investigation.

4 Conclusions

Ruddlesden–Popper-type compounds are particularly attractive electrode materials for fluoride-ion batteries. Among them, $LaSrMnO_4$ has received significant attention due to its high fluoride incorporation capability and lower environmental impact compared to nickel- and cobalt-based analogues. However, direct experimental visualization of fluoride ion motion and the associated energy have been missing. In this work, we provide the first experimental visualization of fluoride ion diffusion in the system using Maximum Entropy Method and Bond Valence Site Energy analyses, supported by molecular dynamics simulations. All techniques converge on a consistent picture in which fluoride ion transport occurs between first-neighbour sites within the anion layers.

Although oxygen excess is well documented in Ruddlesden–Popper oxides, its impact on fluoride ion transport had not been investigated before. Here, additional simulations performed on oxygen over-stoichiometry compositions show that oxygen ions also become mobile at simulated temperatures above 450 K. Three distinct types of oxygen motion were predicted in oxygen-excess compounds. The first follows the same pathway used by fluoride ions. The second occurs in fluoride-free layers, where an interstitial oxygen replaces an apical oxygen, which then moves into a nearby interstitial site, consistent with the typical oxide ion diffusion pathway observed in oxygen-excess Ruddlesden–Popper oxides used for example as electrodes in solid oxides fuel cells. The third mechanism takes place in fluoride-containing layers, where a fluoride ion replaces an apical oxygen atom that then moves into an interstitial position. This last process is particularly important because it traps the fluoride ion in the apical site, while a slower oxygen ion remains in the fluoride layer, resulting in reduced overall anion mobility.

These observations have direct implications for fluoride ion battery performance. Particularly, when a battery is assembled, excess oxygen ions remain within the oxide material. This directly affects electrochemical performance because excess oxygen decreases the number of available sites for fluoride incorporation during cycling, reducing cathode capacity, and obstructs fluoride ion pathways, leading to slower transport and higher overpotential during operation. Even small oxygen over-stoichiometry significantly hinders fluoride mobility, potentially limiting the electrochemical performance, efficiency, and lifespan of the cell. Considering that over-oxidation of RP-type materials might occur at the particle surface especially, the direct interface between electrolyte and active material might even be affected most severely. Therefore, this work points to the decisive role of a precise control of oxygen content being essential to optimize anion transport and to maximize the electrochemical performance of fluoride-based cathode materials.

Conflicts of interest

There are no conflicts to declare.

This journal is © The Royal Society of Chemistry 2026

Open Access Article. Published on 12 March 2026. Downloaded on 4/3/2026 5:12:45 PM. This article is licensed under a Creative Commons Attribution-NonCommercial 3.0 Unported Licence.

Data availability

The data supporting this article have been included in the article and as part of the supplementary information (SI) section. Supplementary information is available. See DOI: https://doi.org/10.1039/d6ta00453a.

Acknowledgements

We acknowledge ISCRA for awarding this project access to the LEONARDO supercomputer, owned by the EuroHPC Joint Undertaking, hosted by CINECA (Italy), ISCRA project: HP10CRB3Z4. The Institut Laue Langevin (ILL) is acknowledged for beam time allocation at the high resolution two axis diffractometer D2B, proposal number: 5-23-833. OC and XG acknowledge funding by the German Research Foundation (DFG) (ProjectID No. 463184206-SFB 1548).

References

1 M. Li, J. Lu, Z. Chen and K. Amine, 30 Years of Lithium-Ion Batteries, *Adv. Mater.*, 2018, **30**(33), 1800561, DOI: 10.1002/adma.201800561.

2 T. M. Bandhauer, S. Garimella and T. F. Fuller, A Critical Review of Thermal Issues in Lithium-Ion Batteries, *J. Electrochem. Soc.*, 2011, **158**(3), R1, DOI: 10.1149/1.3515880.

3 T. Kim, W. Song, D.-Y. Son, L. K. Ono and Y. Qi, Lithium-Ion Batteries: Outlook on Present, Future, and Hybridized Technologies, *J. Mater. Chem. A*, 2019, **7**(7), 2942–2964, DOI: 10.1039/C8TA10513H.

4 M. A. Nowroozi, I. Mohammad, P. Molaiyan, K. Wissel, A. R. Munnangi and O. Clemens, Fluoride Ion Batteries – Past, Present, and Future, *J. Mater. Chem. A*, 2021, **9**(10), 5980–6012, DOI: 10.1039/D0TA11656D.

5 Y. Wang, X. Yang, Y. Meng, Z. Wen, R. Han, X. Hu, B. Sun, F. Kang, B. Li, D. Zhou, C. Wang and G. Wang, Fluorine Chemistry in Rechargeable Batteries: Challenges, Progress, and Perspectives, *Chem. Rev.*, 2024, **124**(6), 3494–3589, DOI: 10.1021/acs.chemrev.3c00826.

6 A. W. Xiao, G. Galatolo and M. Pasta, The Case for Fluoride-Ion Batteries, *Joule*, 2021, **5**(11), 2823–2844, DOI: 10.1016/j.joule.2021.09.016.

7 J. Jacobs, A. Bivour, V. Sikolenko, H. Kohlmann, T. C. Hansen, J. R. Hester, K. Xu, J. Schmedt Auf Der Günne and S. G. Ebbinghaus, Unveiling the Fluorination Pathway of Ruddlesden–Popper Oxyfluorides: A Comprehensive *In Situ* X-Ray and Neutron Diffraction Study, *J. Am. Chem. Soc.*, 2025, **147**(11), 9739–9751, DOI: 10.1021/jacs.4c18187.

8 M. A. Nowroozi, K. Wissel, M. Donzelli, N. Hosseinpourkahvaz, S. Plana-Ruiz, U. Kolb, R. Schoch, M. Bauer, A. M. Malik, J. Rohrer, S. Ivlev, F. Kraus and O. Clemens, High Cycle Life All-Solid-State Fluoride Ion Battery with La_2NiO_{4+d} High Voltage Cathode, *Commun. Mater.*, 2020, **1**(1), 27, DOI: 10.1038/s43246-020-0030-5.

9 M. A. Nowroozi, S. Ivlev, J. Rohrer and O. Clemens, La_2CoO_4 : A New Intercalation Based Cathode Material for Fluoride Ion Batteries with Improved Cycling Stability, *J. Mater. Chem. A*, 2018, **6**(11), 4658–4669, DOI: 10.1039/C7TA09427B.

10 Y. Wang, K. Yamamoto, Y. Tsujimoto, T. Matsunaga, D. Zhang, Z. Cao, K. Nakanishi, T. Uchiyama, T. Watanabe, T. Takami, H. Miki, H. Iba, K. Maeda, H. Kageyama and Y. Uchimoto, Anion Substitution at Apical Sites of Ruddlesden–Popper-Type Cathodes toward High Power Density for All-Solid-State Fluoride-Ion Batteries, *Chem. Mater.*, 2022, **34**(2), 609–616, DOI: 10.1021/acs.chemmater.1c03189.

11 V. Vanita, G. Mezzadra, C. Tealdi and O. Clemens, Fluoride Ion Transport and Phase Evolution in the Cathode Material $LaSrMnO_4$ within All-Solid-State Fluoride Ion Batteries, *ACS Appl. Energy Mater.*, 2025, **8**, 7562–7574, DOI: 10.1021/acsaem.5c00875.

12 H. Miki, K. Yamamoto, H. Nakaki, T. Yoshinari, K. Nakanishi, S. Nakanishi, H. Iba, J. Miyawaki, Y. Harada, A. Kuwabara, Y. Wang, T. Watanabe, T. Matsunaga, K. Maeda, H. Kageyama and Y. Uchimoto, Double-Layered Perovskite Oxyfluoride Cathodes with High Capacity Involving O–O Bond Formation for Fluoride-Ion Batteries, *J. Am. Chem. Soc.*, 2024, **146**(6), 3844–3853, DOI: 10.1021/jacs.3c10871.

13 H. Miki, T. Matsunaga, Z. Li, Z. Cao, K. Yamamoto, M. Kumar, N. Thakur, T. Watanabe, H. Iba, S. Kobayashi, S. Kawaguchi, K. Ikeda, M. Hagihala, T. Kamiyama, A. Kuwabara, H. Kageyama, K. Maeda and Y. Uchimoto, Fluoride Ion Storage and Conduction Mechanism in Fluoride Ion Battery Positive Electrode, Ruddlesden–Popper-Type Layered Perovskite $La_{1.2}Sr_{1.8}Mn_2O_7$ Crystal, *Inorg. Chem.*, 2024, **63**(49), 23095–23102, DOI: 10.1021/acs.inorgchem.4c02341.

14 L. D. Aikens, L. J. Gillie, R. K. Li and C. Greaves, Staged Fluorine Insertion into Manganese Oxides with Ruddlesden–Popper Structures: $LaSrMnO_4F$ and $La_{1.2}Sr_{1.8}Mn_2O_7F$, *J. Mater. Chem.*, 2002, **12**(2), 264–267, DOI: 10.1039/b105550j.

15 M. A. Nowroozi, K. Wissel, J. Rohrer, A. R. Munnangi and O. Clemens, $LaSrMnO_4$: Reversible Electrochemical Intercalation of Fluoride Ions in the Context of Fluoride Ion Batteries, *Chem. Mater.*, 2017, **29**(8), 3441–3453, DOI: 10.1021/acs.chemmater.6b05075.

16 P. Ding, W. Li, H. Zhao, C. Wu, L. Zhao, B. Dong and S. Wang, Review on Ruddlesden–Popper Perovskites as Cathode for Solid Oxide Fuel Cells, *J. Phys. Mater.*, 2021, **4**(2), 022002, DOI: 10.1088/2515-7639/abe392.

17 T. Nakamura, R. Oike, Y. Ling, Y. Tamenori and K. Amezawa, The Determining Factor for Interstitial Oxygen Formation in Ruddlesden–Popper Type La_2 NiO_4 -Based Oxides, *Phys. Chem. Chem. Phys.*, 2016, **18**(3), 1564–1569, DOI: 10.1039/C5CP05993C.

18 AAC TOPAS, TOPAS-Academic: An Optimization Program Integrating Computer Algebra and Crystallographic Objects Written in C++, *J. Appl. Crystallogr.*, 2018, **51**(1), 210–218, DOI: 10.1107/S1600576718000183.

19 K. Momma, T. Ikeda, A. A. Belik and F. Izumi, Dysnomia, a Computer Program for Maximum-Entropy Method

Open Access Article. Published on 12 March 2026. Downloaded on 4/3/2026 5:12:45 PM. This article is licensed under a Creative Commons Attribution-NonCommercial 3.0 Unported Licence.

(MEM) Analysis and Its Performance in the MEM-Based Pattern Fitting, *Powder Diffr.*, 2013, **28**(3), 184–193, DOI: 10.1017/S088571561300002X.

20 H. Chen, L. L. Wong and S. Adams, *SoftBV* – a Software Tool for Screening the Materials Genome of Inorganic Fast Ion Conductors, *Acta Crystallogr., Sect. B: Struct. Sci., Cryst. Eng. Mater.*, 2019, **75**(1), 18–33, DOI: 10.1107/S2052520618015718.

21 K. Momma and F. Izumi, VESTA: A Three-Dimensional Visualization System for Electronic and Structural Analysis, *J. Appl. Crystallogr.*, 2008, **41**(3), 653–658, DOI: 10.1107/S0021889808012016.

22 I. Batatia; P. Benner; Y. Chiang; A. M. Elena; D. P. Kovács; J. Riebesell; X. R. Advincula; M. Asta; M. Avaylon; W. J. Baldwin; F. Berger; N. Bernstein; A. Bhowmik; F. Bigi; S. M. Blau; V. Cărare; M. Ceriotti; S. Chong; J. P. Darby; S. De; F. D. Pia; V. L. Deringer; R. Elijošius; Z. El-Machachi; F. Falcioni; E. Fako; A. C. Ferrari; J. L. A. Gardner; M. J. Gawkowski; A. Genreith-Schriever; J. George; R. E. A. Goodall; J. Grandel; C. P. Grey; P. Grigorev; S. Han; W. Handley; H. H. Heenen; K. Hermansson; C. Holm; C. H. Ho; S. Hofmann; J. Jaafar; K. S. Jakob; H. Jung; V. Kapil; A. D. Kaplan; N. Karimitari; J. R. Kermode; P. Kourtis; N. Kroupa; J. Kullgren; M. C. Kuner; D. Kuryla; G. Liepuoniute; C. Lin; J. T. Margraf; I.-B. Magdău; A. Michaelides; J. H. Moore; A. A. Naik; S. P. Niblett; S. W. Norwood; N. O'Neill; C. Ortner; K. A. Persson; K. Reuter; A. S. Rosen; L. A. M. Rosset; L. L. Schaaf; C. Schran; B. X. Shi; E. Sivonxay; T. K. Stenczel; V. Svahn; C. Sutton; T. D. Swinburne; J. Tilly; C. van der Oord; S. Vargas; E. Varga-Umbrich; T. Vegge; M. Vondrák; Y. Wang; W. C. Witt; T. Wolf; F. Zills; G. Csányi, A Foundation Model for Atomistic Materials Chemistry, arXiv, 2025. doi: DOI: 10.48550/arXiv.2401.00096.

23 A. P. Thompson, H. M. Aktulga, R. Berger, D. S. Bolintineanu, W. M. Brown, P. S. Crozier, P. J. In 'T Veld, A. Kohlmeyer, S. G. Moore, T. D. Nguyen, R. Shan, M. J. Stevens, J. Tranchida, C. Trott and S. J. Plimpton, LAMMPS - a Flexible Simulation Tool for Particle-Based Materials Modeling at the Atomic, Meso, and Continuum Scales, *Comput. Phys. Commun.*, 2022, **271**, 108171, DOI: 10.1016/j.cpc.2021.108171.

24 W. Humphrey, A. Dalke and K. Schulten, VMD: Visual Molecular Dynamics, *J. Mol. Graphics*, 1996, **14**(1), 33–38, DOI: 10.1016/0263-7855(96)00018-5.

25 G. Goret, B. Aoun and E. Pellegrini, MDANSE: An Interactive Analysis Environment for Molecular Dynamics Simulations, *J. Chem. Inf. Model.*, 2017, **57**(1), 1–5, DOI: 10.1021/acs.jcim.6b00571.

26 M. Yashima, N. Sirikanda and T. Ishihara, Crystal Structure, Diffusion Path, and Oxygen Permeability of a Pr_2NiO_4 -Based Mixed Conductor $(Pr_{0.9}La_{0.1})_2(Ni_{0.74}Cu_{0.21}Ga_{0.05})O_{4+\delta}$, *J. Am. Chem. Soc.*, 2010, **132**(7), 2385–2392, DOI: 10.1021/ja909820h.

27 L. Zhang, F. Yao, J. Meng, W. Zhang, H. Wang, X. Liu, J. Meng and H. Zhang, Oxygen Migration and Proton Diffusivity in Transition-Metal (Mn, Fe, Co, and Cu) Doped Ruddlesden–Popper Oxides, *J. Mater. Chem. A*, 2019, **7**(31), 18558–18567, DOI: 10.1039/C9TA05893A.

28 A. Kushima, D. Parfitt, A. Chroneos, B. Yildiz, J. A. Kilner and R. W. Grimes, Interstitialcy Diffusion of Oxygen in Tetragonal $La_2CoO_{4+\delta}$, *Phys. Chem. Chem. Phys.*, 2011, **13**(6), 2242–2249, DOI: 10.1039/C0CP01603A.

29 D. Lee and H. Lee, Controlling Oxygen Mobility in Ruddlesden–Popper Oxides, *Materials*, 2017, **10**(4), 368, DOI: 10.3390/ma10040368.

30 W. Xie, Y.-L. Lee, Y. Shao-Horn and D. Morgan, Oxygen Point Defect Chemistry in Ruddlesden–Popper Oxides $(La_{1-x}Sr_x)_2MO_{4\pm\delta}$ (M = Co, Ni, Cu), *J. Phys. Chem. Lett.*, 2016, **7**(10), 1939–1944, DOI: 10.1021/acs.jpclett.6b00739.

31 T. H. Aalto, J. Jacobs, F. Frey, D. Schiewe and O. Clemens, Gas Evolution in Ruddlesden–Popper-Type Intercalation Cathodes in All-Solid-State Fluoride-Ion-Batteries: Implications on Battery Performance and Synthesis of Highly Oxidized Oxyfluorides, *J. Mater. Chem. A*, 2026, **14**, 1123–1135, DOI: 10.1039/D5TA07033C.